Efficient Deconvolution of Ground-Penetrating Radar Data

Cedric Schmelzbach and Emanuel Huber

***Abstract*—The time (vertical) resolution enhancement of ground-penetrating radar (GPR) data by deconvolution is a long-standing problem due to the mixed-phase characteristics of the source wavelet. Several approaches have been proposed, which take the mixed-phase nature of the GPR source wavelet into account. However, most of these schemes are usually laborious and/or computationally intensive and have not yet found widespread use. Here, we propose a simple and fast approach to GPR deconvolution that requires only a minimal user input. First, a trace-by-trace minimum-phase (spiking) deconvolution is applied to remove the minimum-phase part of the mixed-phase GPR wavelet. Then, a global phase rotation is applied to maximize the sparseness (kurtosis) of the minimum-phase deconvolved data to correct for phase distortions that remain after the minimum-phase deconvolution. Applications of this scheme to synthetic and field data demonstrate that a significant improvement in image quality can be achieved, leading to deconvolved data that are a closer representation of the underlying reflectivity structure than the input or minimum-phase deconvolved data. Synthetic-data tests indicate that, because of the temporal and spatial correlation inherent in the GPR data due to the frequency- and wavenumber-bandlimited nature of the GPR source wavelet and the reflectivity structure, a significant number of samples are required for a reliable sparseness (kurtosis) estimate and stable phase rotation. This observation calls into question the blithe application of kurtosis-based methods within short time windows such as that for time-variant deconvolution.**

***Index Terms*—Deconvolution, ground-penetrating radar (GPR), inverse filtering, signal processing.**

I. Introduction

SURFACE-based ground-penetrating radar (GPR) reflection imaging is a well-established tool for high-resolution subsurface investigation (e.g., [1]–[9]). The detailed stratigraphic interpretation of GPR reflection images critically depends on the accuracy and optimized temporal resolution of the recordings. Unprocessed GPR data can only provide a distorted image of the subsurface because of the suboptimal shape of the wavelet embedded in the data (e.g., [10]). This embedded wavelet is not an ideal delta function spike but is modified by the transmitter-pulse shape (e.g., [11] and [12]), the antenna-to-ground-coupling (e.g., [13]), and the filtering effect of the Earth. All of these factors introduce amplitude distortions and time delays relative to the Earth's true reflectivity structure (impulse response).

Convolution is a linear mathematical operation that is widely used to model wave propagation in 1-D Earth models (e.g., [14] and [15]). In the time domain, convolution can be illustrated with the superposition principle; given an arbitrary time series of spikes with different amplitudes and occurrence times representing, for example, the Earth's reflectivity structure and a wavelet, a convolved trace (model of the GPR trace) can be obtained by shifting a replica of the wavelet to the occurrence time of a spike, scaling it by the amplitude of the spike, and adding it to the output trace. Closely spaced spikes may lead to overlapping (interfering) waveforms. Deconvolution is the inverse operation of convolution and aims at recovering from the convolved trace the spike series given the wavelet. Under noise-free conditions, the spike series can be recovered perfectly, which means that also interference patterns due to closely spaced spikes will be perfectly resolved. Noise, however, affects deconvolution in that only a frequency-bandlimited version of the spike series can be recovered.

Deconvolution is an inverse-filtering technique used to increase the temporal (vertical) resolution of reflection data by removing the embedded wavelet (all deleterious filtering effects described previously) and recovering an estimate of the underlying reflectivity series [14]. Deconvolution is widely considered to be a key step in seismic reflection processing for resolution enhancement (e.g., [15]). Inverse filtering may be carried out as statistical deconvolution (spiking and predictive deconvolution; e.g., [14]–[16]), deterministic, wavelet, or signature deconvolution (e.g., [17] and [18]), or blind deconvolution (e.g., [19]). In contrast to seismic exploration, only a few reports of successful GPR data deconvolution have been published to date using standard deconvolution techniques (e.g., [20]–[22]), deterministic deconvolution employing estimates of the emitted or embedded wavelet [23]–[30], or blind-deconvolution approaches (e.g., [31]–[34]). The lack of reliable deconvolution procedures for GPR data is unsatisfactory because the image accuracy and temporal resolution of many GPR data sets could be further improved.

Standard spiking and predictive deconvolution are based on the assumption that the embedded wavelet is minimum phase (i.e., the energy distribution of the wavelet is as much front-loaded as possible for the given amplitude spectrum and the restriction of causality). However, GPR antennas usually radiate mixed-phase wavelets with maximum amplitudes roughly in the center of the wavelet [5]. This discrepancy in energy

Manuscript received October 18, 2014; revised January 21, 2015; accepted March 21, 2015.

C. Schmelzbach is with Department of Earth Sciences, Institute of Geophysics, ETH Zurich, 8092 Zurich, Switzerland (e-mail: cedric.schmelzbach@erdw.ethz.ch).

E. Huber is with Applied and Environmental Geology, University of Basel, 4056 Basel, Switzerland (e-mail: emanuel.huber@unibas.ch).

Color versions of one or more of the figures in this paper are available online at http://ieeexplore.ieee.org.

Digital Object Identifier 10.1109/TGRS.2015.2419235

distribution (phase characteristics) is likely responsible for the often poor performance reported for standard deconvolution applied to GPR data [28].

In contrast to standard deconvolution approaches, blind-deconvolution techniques involve less restrictive assumptions or none at all about the wavelet phase spectrum (e.g., [35]). Rather, the deconvolution process is constrained by introducing additional assumptions on the reflectivity series itself. For example, the reflectivity series may be assumed to be sparse, which means that the reflectivity series has a higher probability of extreme values compared to a Gaussian (normal) distribution. Kurtosis is a statistical measure to describe the probability distribution of a real-valued random variable; high kurtosis values are found for distributions that are more tail-loaded (sparser; more extreme values) than a Gaussian distribution. Non-Gaussian distributions of (seismic) reflection coefficients have been observed for a wide range of rock sequences [36]. The assumption of a sparse reflection coefficient distribution likely also holds for the electromagnetic case and hence may be used in the context of GPR deconvolution.

In reflection seismology, several deconvolution and data enhancement approaches based on maximizing the kurtosis of the deconvolution output have been presented (e.g., [19], [37]–[42]). For example, [30] applied the time-varying phase-correction technique of [41] to GPR data, which had been previously deconvolved deterministically with an estimated reference wavelet.

Here, we present a GPR deconvolution technique that requires only a minimal user input yet allows for an effective inverse filtering (deconvolution) of mixed-phase GPR data. We begin by demonstrating that a mixed-phase GPR wavelet can be decomposed into its uniquely determined minimum-phase equivalent and an all-pass filter. An all-pass filter is a pure phase-shift filter with unit amplitude spectrum. It passes the amplitude spectrum unaltered but changes the phase spectrum by applying frequency-dependent delays (e.g., [14]). We then show that, in most cases, the phase spectrum of the all-pass component can be approximated by a linear function corresponding to a time shift and a phase rotation term. This lends itself to a simple and efficient deconvolution approach for GPR data. Using a standard spiking deconvolution, the minimum-phase equivalent of the embedded GPR can readily be estimated from the reflection data and be removed. Then, in an automatic search for the sparsest possible solution, the phase rotation angle is sought, which maximizes the kurtosis of the deconvolution output and corrects for any remaining phase distortion. Finally, we demonstrate the efficacy of our scheme for a realistic synthetic 2-D finite-difference data set and a field data set.

II. Methodology

A. Theory

We assume that a GPR trace $x(t)$ represents the convolution of a reflectivity series $r(t)$ with a stationary wavelet $w(t)$ plus some noise $n(t)$ (e.g., [14])

$$x(t) = r(t) * w(t) + n(t) \tag{1}$$

where $*$ denotes convolution and t represents time. For further analysis, we assume that $n(t)$ and $r(t)$ are uncorrelated and that the variance of $n(t)$ is much smaller than the variance of $r(t)$, and therefore, we ignore $n(t)$.

A mixed-phase wavelet $w(t)$ can be decomposed into a minimum-phase wavelet $m(t)$ convolved with a causal dispersive all-pass filter $p(t)$ (canonical representation of a wavelet; [14], [43], [44])

$$w(t) = m(t) * p(t). \tag{2}$$

We can therefore view $m(t)$ as the minimum-phase equivalent of $w(t)$. In the frequency domain, the canonical representation is

$$|W(f)|\, e^{i\phi_w(f)} = |M(f)|\, e^{i\phi_m(f)}\, |P(f)|\, e^{i\phi_p(f)} \tag{3}$$

where f denotes frequency and $|W(f)|$, $|M(f)|$, and $|P(f)|$, and $\phi_w(f)$, $\phi_m(f)$, and $\phi_p(f)$ are the amplitude and phase spectra of $w(t)$, $m(t)$, and $p(t)$. $|P(f)|$ is unity, and $|W(f)|$ is equal to $|M(f)|$. The action of $p(t)$ is contained exclusively in the phase spectrum $\phi_p(f)$.

Given (1), the deconvolution objective is to compute an inverse filter $f(t)$ that converts $w(t)$ into a spike at the origin $\delta(t) = f(t) * w(t)$, where $\delta(t)$ is 1 for $t = 0$ and 0 for $t \neq 0$. Employing (2), the inverse filter for the mixed-phase deconvolution is

$$f_{\text{mixed}}(t) = w^{-1}(t) = m^{-1}(t) * p^{-1}(t). \tag{4}$$

Note that $m^{-1}(t)$ is minimum-phase and causal but $p^{-1}(t)$ is purely noncausal ($p^{-1}(t)$ is a time-reversed version of the causal $p(t)$ mirrored at $t = 0$).

B. Implementation

The canonical representation of a wavelet [(2) and (3)] has been used to estimate mixed-phase wavelets [33], [45]–[48]. These schemes differ in the way the individual components are found, but all use computationally expensive schemes to find the mixed-phase wavelet. Here, we demonstrate that the representation of $\phi_p(f)$ as a linear function is a sufficiently good approximation for wavelet estimation and deconvolution of GPR data. The components of $\phi_p(f)$ can then be found by an automatic search and involve minimal user input.

By taking advantage of the canonical decomposition of a mixed-phase wavelet, the estimation of $w^{-1}(t)$ (4) can be carried out in two steps. First, $m^{-1}(t)$ is estimated from a recorded data trace $x(t)$ by, for example, solving the normal equations using the autocorrelation function (ACF) of $x(t)$. In principle, this procedure corresponds to applying a standard minimum-phase spiking deconvolution (e.g., [15]), requiring as user input the determination of an estimation time window and the definition of the inverse filter length. Once $m^{-1}(t)$ is computed, $m(t)$ is found by solving a second time the normal equations using the ACF of $m^{-1}(t)$.

Second, $p^{-1}(t)$ has to be estimated (4), which involves determining the phase spectrum $\phi_p(f)$ (3). Here, we assume that $\phi_p(f)$ can be approximated by a linear function

$$\phi_p(f) = \phi_{\text{rot}} + bf. \tag{5}$$

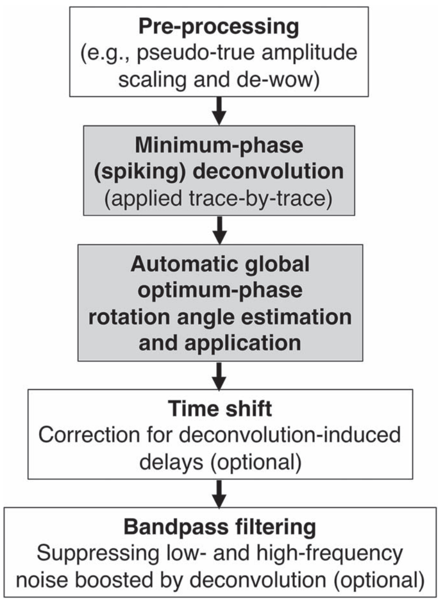

Fig. 1. Processing scheme for GPR deconvolution. The elementary deconvolution steps are shown in light-gray boxes, and optional pre- and postprocessing steps are shown in white boxes.

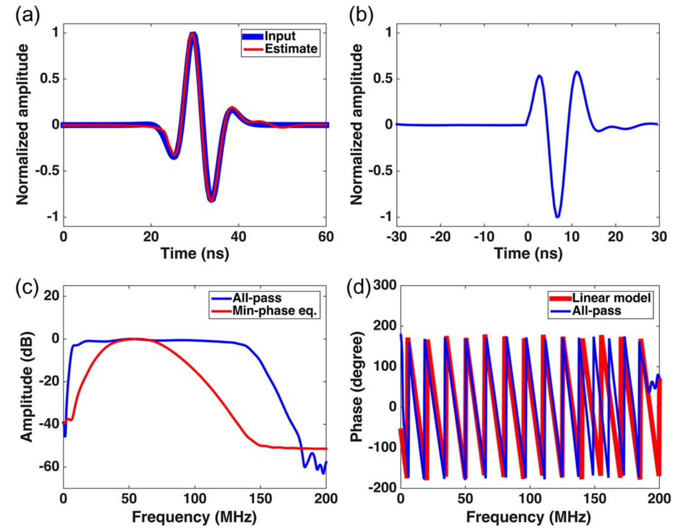

Fig. 2. Synthetic data example. (a) Input and estimated mixed-phase GPR wavelet. (b) Estimated minimum-phase equivalent of the input wavelet shown in (a). (c) Amplitude spectrum of the all-pass filter and minimum-phase equivalent shown in (b). (d) Phase spectrum of the true all-pass filter plotted together with the estimated linear model for the all-pass phase spectrum.

The intercept ϕ_{rot} corresponds to a phase rotation, whereas the slope b relates to a time shift $\tau = b/(2\pi f)$. Applying a fixed (constant) phase rotation changes the shape of a wavelet. For example, $\phi_{\mathrm{rot}} = 90^{\circ}$ converts a symmetric wavelet into an antisymmetric wavelet, whereas $\phi_{\mathrm{rot}} = 180^{\circ}$ corresponds to a polarity change. A phase rotation is conveniently applied to a trace $x(t)$ by employing the Hilbert transform of the trace $H(x(t))$

$$x_{\mathrm{rot}}(t) = x(t)\cos(\phi_{\mathrm{rot}}) - H\left(x(t)\right)\sin(\phi_{\mathrm{rot}}). \tag{6}$$

In order to find the optimum $\phi_{\mathrm{rot}}^{\mathrm{opt}}$, we apply a suite of phase shifts to the data after inverse minimum-phase filtering and seek the sparsest possible output. Thereby, it is sufficient to scan the rotation angle range from 0°–180°. We use the kurtosis k to measure the sparseness (e.g., [38] and [49])

$$k = \frac{\frac{1}{n}\sum_{j=1}^{n}(x_j - \overline{x})^4}{\left(\frac{1}{n}\sum_{j=1}^{n}(x_j - \overline{x})^2\right)^2} \tag{7}$$

where $\overline{x}$ is the mean of all samples and j denotes the sample index. The kurtosis is a statistical measure to describe the shape of a distribution. A Gaussian distribution has a kurtosis value of 3; distributions with more extreme values than the Gaussian distribution have higher kurtosis values. Once $\phi_{\mathrm{rot}}^{\mathrm{opt}}$ is found, an estimate of $w(t)$ can be obtained by applying a phase shift of $-\phi_{\mathrm{rot}}^{\mathrm{opt}}$ to $m(t)$. A remaining time shift τ will delay the deconvolved output relative to the underlying reflectivity structure. Borehole information can, for example, be used to correct for this delay. However, we deem the delay τ for most GPR applications as unimportant because the interpretation of GPR images is usually done in time relative to the first arrivals (air/ground wave). The processing flow for applying the GPR deconvolution scheme proposed here is summarized in Fig. 1.

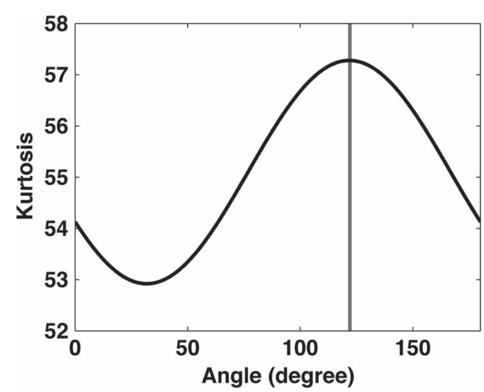

Fig. 3. Kurtosis values plotted against the rotation angle from a sequential application of phase rotations to the minimum-phase equivalent shown in Fig. 2(b). The maximum kurtosis value is found for a rotation angle of 122°.

III. Synthetic Data Example: Mixed-Phase Wavelet Estimation

In the following, we demonstrate the application of the wavelet estimation and deconvolution procedure based on the canonical model and employing a linear phase model on a simple but realistic GPR wavelet. The goal is to reconstruct the wavelet shown in Fig. 2(a) by applying the workflow outlined previously (Fig. 1). The minimum-phase equivalent was found by solving the normal equations twice [Fig. 2(b)]. A sequential application of phase rotations to the minimum-phase equivalent [Fig. 2(b)] revealed that a phase shift of 122° yielded the highest kurtosis value (Fig. 3). The resultant estimated mixed-phase wavelet after phase rotation very closely matches the input waveform [red line in Fig. 2(a)].

In order to verify that a simple phase rotation is a sufficient representation of the all-pass filter, we estimated the true all-pass filter by dividing the Fourier spectrum of the input

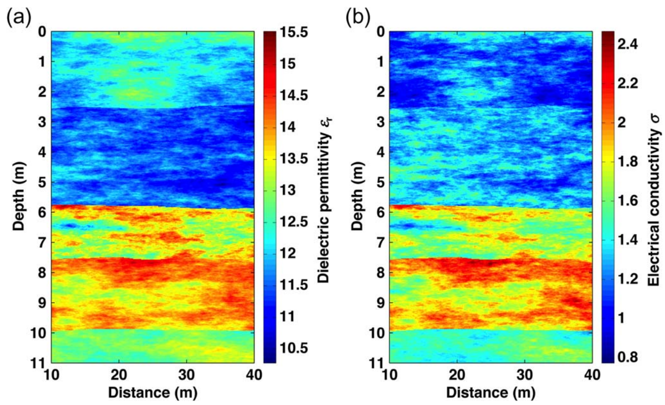

Fig. 4. Physical parameter models for the 2-D finite-difference modeling. (a) Dielectric permittivity (ϵ_r) model. (b) Electrical conductivity (σ) model.

wavelet by the Fourier spectrum of the minimum-phase equivalent. The amplitude and phase spectra of the all-pass filter are displayed in Fig. 2(c) and (d), respectively. The amplitude spectrum of the all-pass filter is flat, as expected over the signal bandwidth of ∼20–120 MHz [Fig. 2(c)]. The phase spectrum closely matches a linear function of frequency: $\phi(f) = -58^\circ + (-24\ \frac{^\circ}{\mathrm{MHz}})f$ [Fig. 2(d)]. The intercept of -58° corresponds, after correcting for the cyclic nature of the phase spectrum, to 122° as found by the kurtosis maximization. The slope (-24 °/MHz) corresponds to a time shift, which has to be defined by the user.

The observation that a short-duration mixed-phase wavelet can be decomposed into its minimum-phase equivalent and an all-pass filter with a simple linear phase spectrum is likely applicable to other GPR cases because short-duration wavelets are produced by many pulsed GPR transmitters (e.g., [11] and [12]). Short pulses have a broad and smooth amplitude spectrum and consequently also a simple and smooth phase spectrum.

IV. Realistic 2-D Synthetic Data Example

Electromagnetic wave propagation depends not only on the medium dielectric permittivity (ϵ_r) distribution, which primarily controls the wave speed and reflectivity, but also on the medium electrical conductivity (σ) distribution. The conductivity σ and its changes in the subsurface are responsible for attenuation and complex reflection coefficients (e.g., [5]), which can affect the stationarity of the input traces. However, the convolutional model [(1)] underlying the deconvolution scheme requires that the wavelet is stationary.

We tested our GPR deconvolution technique on realistic synthetic data by generating noise-free GPR recordings employing a 2-D finite-difference time-domain solution of Maxwell's equations [50]. Fig. 4(a) and (b) displays the sections of ϵ_r and σ models, respectively, that simulate a realistic water-saturated sand aquifer represented by a layered background with stochastic fine-scale structures superimposed. The stochastic variations are defined by von Kármán autocovariance functions [51], [52] with horizontal and vertical correlation lengths of 20 and 1 m, respectively, leading to predominantly horizontal stratification (e.g., [53]). The ϵ_r and σ values range from 10.3 to 15.5 and from 0.8 to 2.5 mS/m, with average values of 12.7 and 1.5 mS/m, respectively, which we consider realistic for saturated clay-free sediments.

We calculated a surface reflection 100-MHz GPR data set collected over the ϵ_r and σ models by moving a pair of transmitter and receiver antennas separated by 1 m in 0.1-m increments. The emitted source signal was a truncated Ricker wavelet with a central (peak) frequency of 100 MHz. Data preprocessing involved muting the highly energetic air and ground waves, and scaling the amplitudes by applying a spherical-spreading correction and an exponential-gain function. An enlarged portion of the scaled data is shown in Fig. 5(a). The estimation of the spiking-deconvolution operator $m^{-1}(t)$ requires a time window that is long enough to allow for a stable estimation of the spectral properties of the operator from data. This time window should primarily contain signals (reflections). It is therefore necessary to exclude noise-dominated parts of the GPR section such as the air/ground waves and late times dominated by random noise. Because the penetration depth of GPR is limited and recording times may be short, we suggest combining the data within signal windows of several adjacent traces into one "supertrace" for a stable operator estimation but still applying the operator to the central trace only. For the synthetic example discussed here, we selected a time window ranging from 50 to 300 ns for the estimation of $m^{-1}(t)$ and combined 11 adjacent traces for stabilizing the filter estimation.

A comparison of the input data after minimum-phase (spiking) deconvolution [Fig. 5(b)] with the bandlimited reflectivity section (reflectivity derived from the ϵ_r model and bandpass filtered to the same frequency content as the deconvolution output) shows that minimum-phase deconvolution improves the resolution (sharpness) of the data. However, the data are contaminated by a residual phase error that is clearly visible when comparing, for example, the subhorizontal reflection at ∼130 ns between Fig. 5(b) and (d). Also, a trace-to-trace comparison of the minimum-phase deconvolved data with the bandlimited reflectivity shown in Fig. 6(b) illustrates the remaining phase error in the minimum-phase deconvolved data.

A reliable estimation of the kurtosis requires a large number of samples (e.g., [33] and [38]). We therefore estimate one global residual phase correction for all traces within the signal window (50–300 ns). The GPR deconvolution output after 50–250 MHz bandpass filtering and a phase rotation of 92° of the minimum-phase deconvolution output is displayed in Fig. 5(c). The deconvolved data were shifted in time to match the bandlimited reflectivity section. A comparison of the GPR deconvolution output [Fig. 5(c)] with the bandlimited reflectivity [Fig. 5(d)] and with the input data [Fig. 5(a)] highlights that GPR deconvolution significantly increased the vertical resolution and resulted in a section that more closely represents the underlying reflectivity structure. The averaged normalized cross-correlation between all collocated traces of the bandlimited reflectivity section and 1) the input data, 2) the minimum-phase deconvolved section, and 3) the GPR deconvolved section is on average -0.05, 0.61, and 0.76, respectively. These similarity values illustrate that GPR deconvolution improved to the fit of the processed data to the bandlimited reflectivity.

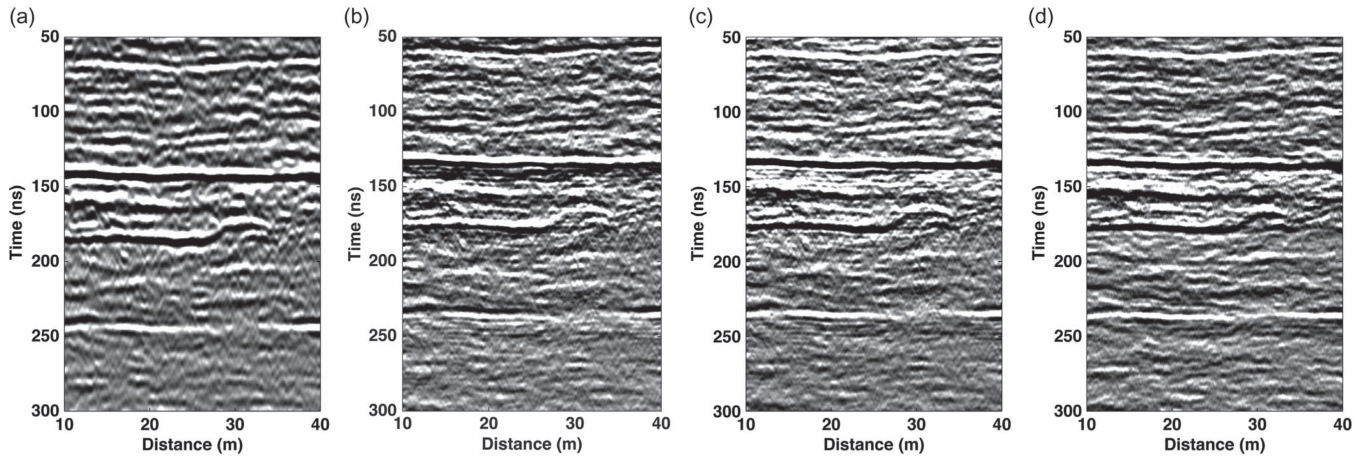

Fig. 5. (a) Synthetic data generated using a 2-D finite-difference modeling scheme from the physical parameter models shown in Fig. 4 after amplitude scaling. (b) Minimum-phase (spiking) deconvolution of (a). (c) GPR deconvolution of (a). (d) Bandlimited reflectivity computed from the dielectric permittivity model shown in Fig. 4(a).

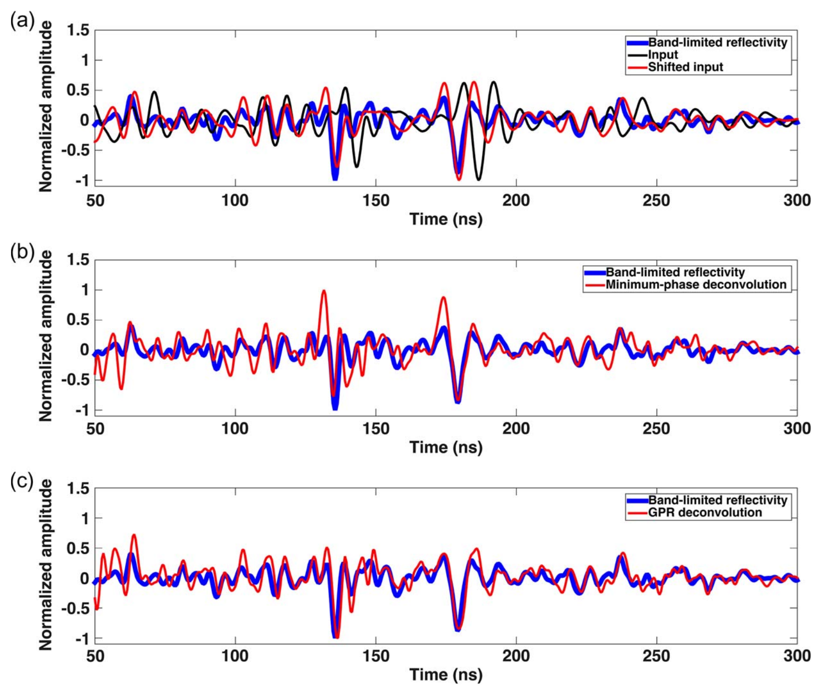

Fig. 6. Traces extracted at 25-m distance from the synthetic data shown in Fig. 5. (a) Bandlimited reflectivity, input data, and inputted data trace shifted to match the bandlimited reflectivity. (b) Bandlimited reflectivity and minimum-phase (spiking) deconvolution output. (c) Bandlimited reflectivity and GPR deconvolution output.

Note that the lower correlation value of the minimum-phase deconvolved traces compared to the GPR deconvolved traces is solely due to the remaining phase error after minimum-phase deconvolution.

These observations are confirmed by the trace-to-trace comparison displayed in Fig. 6; the deconvolved trace extracted from Fig. 5(c) matches the bandlimited reflectivity closer than the input data (e.g., at 125 and 175 ns). Note that the black line in Fig. 6(a) represents the trace extracted from the input trace data [Fig. 5(a)], whereas the red line corresponds to the input data shifted to match the bandlimited reflectivity (blue line) to facilitate the comparison. Furthermore, the average of all estimated mixed-phase wavelets matches the emitted source wavelet (first derivative of the injected source current) very well (Fig. 7).

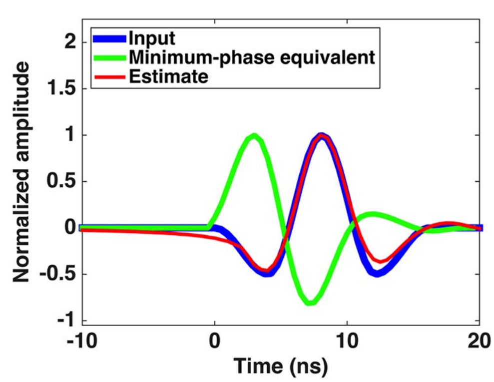

Fig. 7. Emitted wavelet (first derivative of the injected source current in the finite-difference simulation) and average of all estimated minimum-phase equivalents and mixed-phase wavelets.

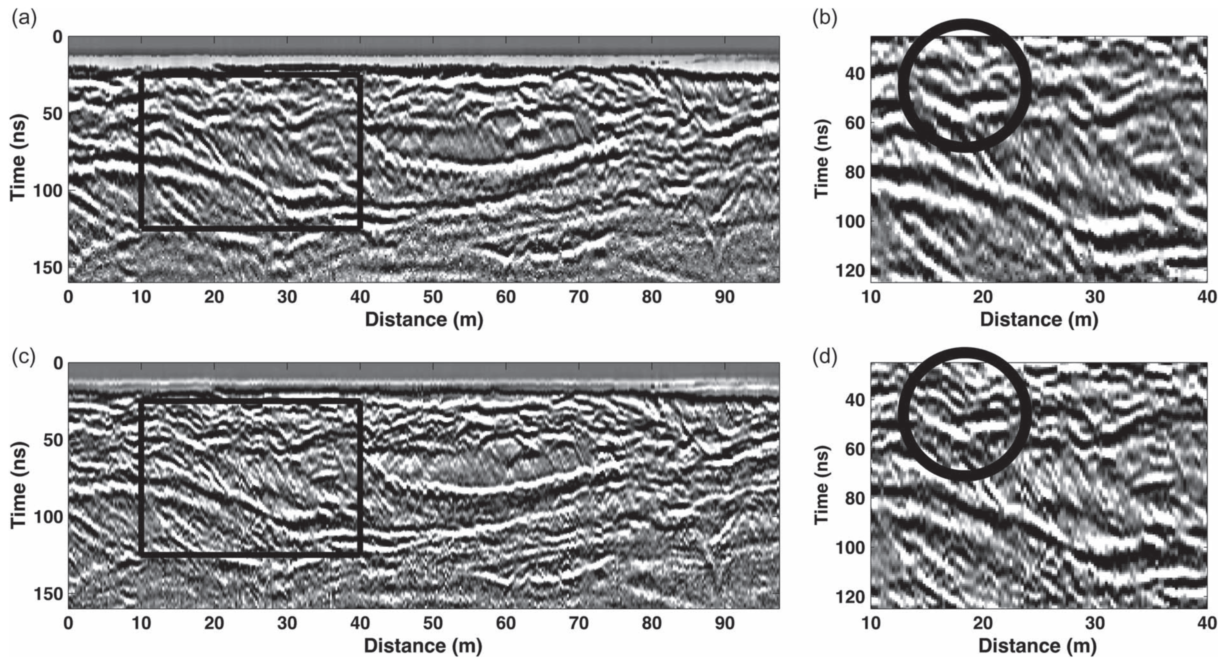

Fig. 8. Application of the GPR deconvolution to a 100-MHz field data set. (a) Data after amplitude scaling. Black box marks zoomed-in portion shown in (b). (c) GPR deconvolution of (a). Black box marks the zoomed-in portion shown in (d). The black circle in (b) and (d) marks an example area of increased resolution.

V. Field Data Application

We applied our GPR deconvolution procedure to a 100-MHz GPR field data set collected over the Tagliamento braid-plain in Northern Italy. The fluvial sediments at the study site consist primarily of gravel and coarse sand. The data were recorded by moving a pair of antennas separated by 1 m along a 100-m-long profile at 25-cm trace spacing (391 traces, 32 stacks, and 0.8-ns sampling interval). Initial processing included interpolating the clipped airwave/ground wave amplitudes, removing the dc shift of each trace, time-zero corrections, spherical-spreading corrections, "de-wow" by high-pass frequency filtering (20–400-MHz passband), and exponential-gain scaling (e.g., [54]). The scaled data show a substantial penetrating depth of around 200 ns ($\sim$10 m depth for a velocity of 0.1 m/s) and an overall high signal-to-noise ratio indicating a favorable environment for GPR imaging [Fig. 8(a)].

For the estimation of the deconvolution operators, we focused on a signal time window ranging from 32 to 112 ns. The window starts just below the air/ground wave, and its length is a tradeoff between maximizing the length and excluding late times, when signals may be affected by absorption and noise. As in the synthetic-data example, $m^{-1}(t)$ was applied trace-by-trace but estimated based on the data from a time-space window including neighboring traces. Parameter testing showed that combining 11 traces helps in stabilizing the estimation of the 35-sample (27.2 ns) spiking-deconvolution operator $m^{-1}(t)$ (see Fig. 9(a) for the minimum-phase equivalent). A rotation angle of 134° provided the highest possible kurtosis value for all traces within the entire signal window. After deconvolution, filtering with a 15–175-MHz passband and scaling each trace by its rms value completed the processing [Fig. 8(c)].

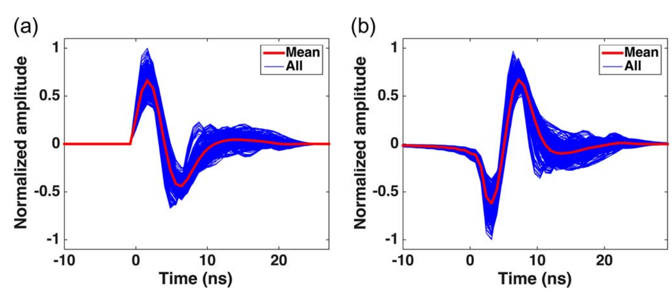

Fig. 9. GPR wavelets estimated from the field data [Fig. 8(a)]. (a) Minimum-phase equivalent estimated for each trace plotted in blue; the average of all estimates is superimposed in red. (b) Mixed-phase wavelet estimated for each trace plotted in blue; the average of all estimates is superimposed in red.

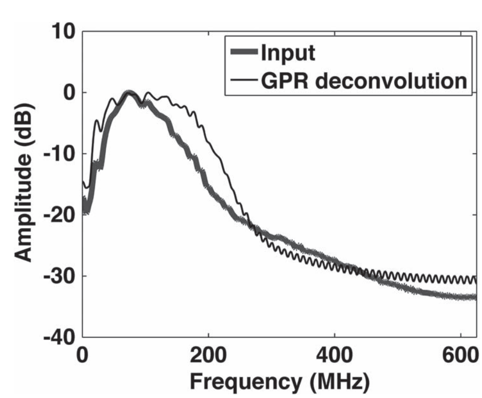

Fig. 10. RMS amplitude spectra of the input section [Fig. 8(a)] and deconvolved section [Fig. 8(b)].

Deconvolution removed the mixed-phase wavelets displayed in Fig. 9(b) from the input data and thereby balanced the amplitude spectrum [Fig. 10]. Compared to the input data

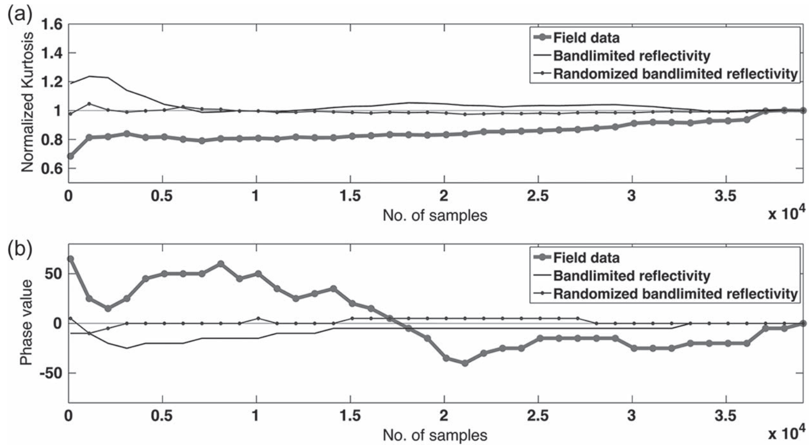

Fig. 11. (a) Normalized kurtosis estimates as a function of increasing sample number for the deconvolved field data [see Fig. 8(c)], model of bandlimited reflectivity (see Fig. 5), and randomized version of the bandlimited reflectivity. Kurtosis values normalized by the corresponding value for 39’100 samples. (b) Phase estimate corresponding to the maximum kurtosis estimate shown in (a).

[Fig. 8(a) and (b)], the deconvolved section [Fig. 8(c) and (d)] shows a significantly improved vertical resolution, and the visibility of interfering events has increased. Note, for example, the improved interpretability and increased amount of discernible details of the fluvial sediments.

VI. Discussion

GPR signals may undergo changes in wavelet shape when propagating through the underground due to, for example, frequency-dependent attenuation and velocity dispersion. Significant changes in the wavelet shape may violate the stationarity assumption underlying the convolutional model (1) and hence lead to suboptimal deconvolution results. Time-variant deconvolution techniques have been proposed to compensate for time-dependent wavelet changes (e.g., [30]). If kurtosis maximization is used for the deconvolution operator design, such as when applying the time-varying phase-correction technique of [41] or [30], kurtosis values may have to be estimated for short time windows or small numbers of samples.

To test the robustness of the kurtosis estimation and resultant phase correction as a function of the number of data samples, we performed the kurtosis maximization and phase-correction procedure outlined previously on data sets with increasing numbers of samples. We started by estimating the optimum phase rotation angle and corresponding kurtosis value for the first trace of the deconvolved field data set and selected the trace portion within the same signal time window as used before, which is 100 samples (80 ns) long. We then analyzed progressively more neighboring traces (combining the traces into one “super-trace”) and re-estimated the phase and kurtosis values.

For comparison, we repeated the same analysis with the synthetic reflectivity model from the tests described earlier (see Figs. 4 and 5). The reflectivity model was bandpass filtered to the same frequency content as the field data, and a 100-sample-long (80 ns; around 8 dominant periods for a dominant frequency of 100 MHz; Fig. 10) signal window was chosen for the analysis. Because the embedded wavelet in both the deconvolved field data and the frequency-bandlimited reflectivity is zero phase, the optimum phase rotation angle for both data sets should be 0°. The kurtosis values of the full 391-trace (39’100 samples) field data and bandlimited reflectivity are 4.6 and 9.6, respectively.

The computed phase rotation and kurtosis values are plotted against the number of samples in Fig. 11(a) and (b), respectively. For both the field data and the bandlimited reflectivity, the kurtosis value of the entire data set (normalized value of 1) is gradually reached with an increasing number of samples. Kurtosis value estimation of a field data set requires a considerable number of samples, 90% of the final value is reached for around 30 000 samples, whereas only around 5 000 samples are needed for the bandlimited reflectivity to reach close to its final value. The evolution of the kurtosis value with the number of samples, as well as the final value, may be strongly influenced by the distribution of the amplitude values within the analysis window. Prominent single reflections will dominate the kurtosis estimation, such as the reflection at around 145 ns in the bandlimited reflectivity (Fig. 5). The resultant field data phase rotation values fluctuate considerably for small sample numbers. The phase value estimates converge to a value of around -15° for $>$25 000 samples. Note that phase rotations with angles of $<15^\circ$ are hardly visible.

GPR sections exhibit vertical as well as lateral correlation (e.g., [55]), which are due to the frequency-bandlimited nature of GPR data and the spatial correlation (spatial bandlimited nature) of the underlying reflectivity. We assessed the influence of temporal and spatial correlation by computing the optimum phase angle and kurtosis for the bandlimited reflectivity model used before but selected the traces randomly. The resultant phase and kurtosis curves show that the full-data kurtosis value and phase angle of 0° are reached with a significantly lower number of samples (around 2000 samples). The comparison with the bandlimited reflectivity highlights the fact that a significant number of samples (number of traces and/or record length) are necessary for a stable kurtosis estimation due to the bandlimited nature of the data. Furthermore, the dependence on wavenumber and frequency band-limitation implies that the success of kurtosis estimation and, hence, the mixed-phase GPR deconvolution described here depends on the frequency bandwidth of the data and the spatial-correlation properties of the subsurface.

VII. Conclusion

Casting the deconvolution problem of GPR data into a form that incorporates the application of a trace-by-trace minimum-phase (spiking) deconvolution followed by a global phase rotation correction to maximize the kurtosis of the GPR data enables a fast and robust resolution enhancement scheme requiring only minimal user input. The key assumptions underlying this scheme are as follows: 1) the signal stationarity within the estimation time window; 2) the sparseness of the reflectivity; and 3) a mixed-phase GPR wavelet can be expressed as the convolution of a minimum-phase wavelet with an all-pass filter that has a linear phase spectrum as a function of frequency. A robust estimation of the kurtosis requires a significant number of samples, with the data frequency bandwidth and the spatial-correlation properties of the underground dictating the amount.

Our GPR deconvolution approach may not only provide enhanced subsurface images with increased accuracy but should also precede any quantitative interpretation of GPR reflection amplitudes (e.g., impedance inversion and amplitude-versus-offset analysis). Our synthetic-data and field data tests showed that the approximation of the all-pass filter phase spectrum with a linear function is sufficient. However, the phase spectrum could also be approximated with other functions. The GPR deconvolution scheme discussed here requires long time series with stationary signals and hence may fail when applied to data from locations with significant frequency-dependent absorption and dispersion. Further developments could, therefore, aim at including time-dependent deconvolution approaches such as Gabor deconvolution. Whereas the examples presented here deal with GPR data, the algorithm may as well be employed to deconvolve (mixed-phase) seismic data.

Acknowledgment

The authors would like to thank S. Greenhalgh for commenting on an earlier draft of this paper and the Associate Editor and three anonymous reviewers for their comments that helped in improving the quality of this paper.

References

[1] M. Beres, A. Green, P. Huggenberger, and H. Horstmeyer, "Mapping the architecture of glaciofluvial sediments with three-dimensional georadar," *Geology*, vol. 23, no. 12, pp. 1087–1090, Dec. 1995.

[2] M. Beres, P. Huggenberger, A. G. Green, and H. Horstmeyer, "Using two- and three-dimensional georadar methods to characterize glaciofluvial architecture," *Sedimentary Geol.*, vol. 129, no. 1/2, pp. 1–24, Nov. 1999.

[3] A. Neal, "Ground-penetrating radar and its use in sedimentology: Principles, problems and progress," *Earth-Sci. Rev.*, vol. 66, no. 3/4, pp. 261–330, Aug. 2004.

[4] R. Gross, A. Green, H. Horstmeyer, and J. Begg, "Location and geometry of the Wellington Fault (New Zealand) defined by detailed three-dimensional georadar data," *J. Geophys. Res.*, vol. 109, no. B5, May 2004, Art. ID. B05401.

[5] A. P. Annan, "Ground-penetrating radar," in *Near-Surface Geophysics*, ser. Investigations in Geophysics, D. K. Butler, Ed. Tulsa, OK, USA: Soc. Exploration Geophys., 2005, no. 13, ch. 11, pp. 357–438.

[6] A. F. McClymont *et al.*, "Visualization of active faults using geometric attributes of 3D GPR data: An example from the Alpine Fault Zone, New Zealand," *Geophysics*, vol. 73, no. 2, pp. B11–B23, Mar./Apr. 2008.

[7] E. Slob, M. Sato, and G. Olhoeft, "Surface and borehole ground-penetrating-radar developments," *Geophysics*, vol. 75, no. 5, pp. 75A103–75A120, Sep. 2010.

[8] C. Schmelzbach, J. Tronicke, and P. Dietrich, "Three-dimensional hydrostratigraphic models from ground-penetrating radar and direct-push data," *J. Hydrol.*, vol. 398, no. 3/4, pp. 235–245, Feb. 2011.

[9] V. Rodriguez *et al.*, "Characterizing sagging and collapse sinkholes in a mantled karst by means of ground penetrating radar (GPR)," *Environ. Eng. Geosci.*, vol. 20, no. 2, pp. 109–132, May 2014.

[10] R. L. van Dam and W. Schlager, "Identifying causes of ground-penetrating radar reflections using time-domain reflectometry and sedimentological analyses," *Sedimentology*, vol. 47, no. 2, pp. 435–449, Apr. 2000.

[11] R. Streich and J. van der Kruk, "Characterizing a GPR antenna system by near-field electric field measurements," *Geophysics*, vol. 72, no. 5, pp. A51–A55, Sep./Oct. 2007.

[12] C. Warren and A. Giannopoulos, "Creating finite-difference time-domain models of commercial ground-penetrating radar antennas using Taguchi's optimization method," *Geophysics*, vol. 76, no. 2, pp. G37–G47, Mar. 2011.

[13] B. Lampe and K. Holliger, "Effects of fractal fluctuations in topographic relief, permittivity and conductivity on ground-penetrating radar antenna radiation," *Geophysics*, vol. 68, no. 6, pp. 1934–1944, Nov. 2003.

[14] E. A. Robinson and S. Treitel, *Geophysical Signal Analysis*. Tulsa, OK, USA: Soc. Exploration Geophys., 2000.

[15] O. Yilmaz, *Seismic Data Analysis. Processing, Inversion, and Interpretation of Seismic Data*, vol. 1/2, Tulsa, OK, USA: Soc. Exploration Geophys., 2001.

[16] E. A. Robinson and S. Treitel, "Principles of digital Wiener filtering," *Geophys. Prospect.*, vol. 15, no. 3, pp. 311–333, Sep. 1967.

[17] A. J. Berkhout, "Least-squares inverse filtering and wavelet deconvolution," *Geophysics*, vol. 42, no. 7, pp. 1369–1383, Dec. 1977.

[18] L. Wood, R. Heiser, S. Treitel, and P. Riley, "The debubbeling of marine source signatures," *Geophysics*, vol. 43, no. 4, pp. 715–729, Jun. 1978.

[19] R. A. Wiggins, "Minimum entropy deconvolution," *Geoexploration*, vol. 16, no. 1/2, pp. 21–35, Apr. 1978.

[20] P. T. Lafleche, J. P. Todoeschuck, O. G. Jensen, and A. S. Judge, "Analysis of ground-probing radar data: Predictive deconvolution," *Can. Geotech. J.*, vol. 28, no. 1, pp. 134–139, Feb. 1991.

[21] S. C. Fisher, R. R. Stewart, and H. M. Jol, "Ground penetrating radar (GPR) data enhancement using seismic techniques," *J. Environ. Eng. Geophys.*, vol. 1, no. 2, pp. 89–96, 1996.

[22] S. A. Arcone, D. E. Lawson, A. J. Delaney, J. C. Strasser, and J. D. Strasser, "Ground-penetrating radar reflection profiling of groundwater and bedrock in an area of discontinuous permafrost," *Geophysics*, vol. 63, no. 5, pp. 1573–1584, Oct. 1998.

[23] F.-M. Gottsche, C. Stolte, and K.-P. Nick, "Two-sided deconvolution—A method to improve the temporal resolution in radar data," presented at the 56th EAGE Meet. Technical Exhibition, Expanded Abstracts, Vienna, Austria, 1994, Paper P049.

[24] F. Neves and J. Miller, "Source signature deconvolution of ground penetrating radar data," in *Proc. 6th Int. Conf. Ground Penetrating Radar*, 1996, pp. 573–578.

[25] J. Xia, E. K. Franseen, R. D. Miller, T. V. Weis, and A. P. Byrnes, "Improving ground-penetrating radar data in sedimentary rocks using deterministic deconvolution," *J. Appl. Geophys.*, vol. 54, no. 1/2, pp. 15–33, Nov. 2003.

[26] J. Xia, E. K. Franseen, R. D. Miller, and T. V. Weis, "Application of deterministic deconvolution of ground-penetrating radar data in a study of carbonate strata," *J. Appl. Geophys.*, vol. 56, no. 3, pp. 213–229, Oct. 2004.

[27] Y.-L. Chen and J. Chow, "Ground penetrating radar signal processing improves mapping accuracy of underground voids and seawater table: An application in deteriorating coastal structure, Nanfangao Port, Taiwan," *Environ. Geol.*, vol. 53, no. 2, pp. 445–455, Oct. 2007.

[28] F. Belina, B. Dafflon, J. Tronicke, and K. Holliger, "Enhancing the vertical resolution of surface georadar data," *J. Appl. Geophys.*, vol. 68, no. 1, pp. 26–35, May 2009.

[29] N. Economou and A. Vafidis, "Deterministic deconvolution for GPR data in the $t-f$ domain," *Near Surf. Geophys.*, vol. 9, no. 5, pp. 427–433, Oct. 2011.

[30] N. Economou and A. Vafidis, "GPR data time varying deconvolution by kurtosis maximization," *J. Appl. Geophys.*, vol. 81, pp. 117–121, Jun. 2012.
[31] M. J. Porsani and B. Ursin, "Mixed-phase deconvolution of seismic and ground penetrating radar data," in *Proc. SEG Tech. Program Expanded Abstracts*, 1996, pp. 1603–1606.
[32] K. Chahine, V. Baltazart, X. Derobert, and Y. Wang, "Blind deconvolution via independent component analysis for thin-pavement thickness estimation using GPR," in *Proc. Int. RADAR Conf. Surveillance Safer World*, 2009, pp. 1–5.
[33] C. Schmelzbach, F. Scherbaum, J. Tronicke, and P. Dietrich, "Bayesian frequency-domain blind deconvolution of ground-penetrating radar data," *J. Appl. Geophys.*, vol. 75, no. 4, pp. 615–630, Dec. 2011.
[34] L. Li, "Sparsity-promoted blind deconvolution of ground-penetrating radar (GPR) data," *IEEE Geosci. Remote Sens. Lett.*, vol. 11, no. 8, pp. 1330–1334, Aug. 2014.
[35] M. D. Sacchi and T. J. Ulrych, "Nonminimum-phase wavelet estimation using higher order statistics," *Leading Edge*, vol. 19, no. 1, pp. 80–83, 2000.
[36] A. T. Walden and J. W. J. Hosken, "The nature of the non-Gaussianity of primary reflection coefficients and its significance for deconvolution," *Geophys. Prospect.*, vol. 34, no. 7, pp. 1038–1066, Nov. 1986.
[37] S. Levy and D. W. Oldenburg, "Automatic phase correction of common-midpoint stacked data," *Geophysics*, vol. 52, no. 1, pp. 51–59, Jan. 1987.
[38] R. E. White, "Maximum kurtosis phase correction," *Geophys. J.*, vol. 95, no. 2, pp. 371–389, Nov. 1988.
[39] D. Donoho, "On minimum entropy deconvolution," in *Applied Time Series Analysis II*, D. F. Findley, Ed. San Diego, CA, USA: Academic, 1981, pp. 565–608.
[40] J. Longbottom, A. T. Walden, and R. E. White, "Principles and application of maximum kurtosis phase estimation," *Geophys. Prospect.*, vol. 36, no. 2, pp. 115–138, Feb. 1988.
[41] M. van der Baan, "Time-varying wavelet estimation and deconvolution by kurtosis maximization," *Geophysics*, vol. 73, no. 2, pp. V11–V18, Mar./Apr. 2008.
[42] M. van der Baan and S. Fomel, "Nonstationary phase estimation using regularized local kurtosis maximization," *Geophysics*, vol. 74, no. 6, pp. A75–A80, Nov./Dec. 2009.
[43] J. F. Claerbout, *Fundamentals of Geophysical Data Processing*. Oxford, U.K.: Blackwell, 1985.
[44] E. A. Robinson and S. Treitel, *Digital Imaging and Deconvolution: The ABCs of Seismic Exploration and Processing*, ser. Geophysical References, vol. 15, Tulsa, OK, USA: Soc. Exploration Geophys., 2008.
[45] M. J. Porsani and B. Ursin, "Mixed-phase deconvolution," *Geophysics*, vol. 63, no. 02, pp. 637–647, Apr. 1998.
[46] B. Ursin and M. J. Porsani, "Estimation of an optimal mixed-phase inverse filter," *Geophys. Prospect.*, vol. 48, no. 4, pp. 663–676, Jul. 2000.
[47] S. Misra and M. D. Sacchi, "Non-minimum phase wavelet estimation by non-linear optimization of all-pass operators," *Geophys. Prospect.*, vol. 55, no. 2, pp. 223–234, Mar. 2007.
[48] C. Schmelzbach and F. Scherbaum, "Bayesian frequency-domain mixed-phase wavelet estimation and deconvolution," presented at the 73rd EAGE Conf. Exhibition, Expanded Abstracts, 2011, Paper F039.
[49] Y. Dodge, *The Oxford Dictionary of Statistical Terms*. London, U.K.: Oxford Univ. Press, 2003.
[50] A. Giannopoulos, "Modelling ground penetrating radar by GprMax," *Construct. Build. Mater.*, vol. 19, no. 10, pp. 755–762, Dec. 2005.
[51] K. Holliger, "Upper-crustal seismic velocity heterogeneity as derived from a variety of P-wave sonic logs," *Geophys. J. Int.*, vol. 125, no. 3, pp. 813–829, Jun. 1996.
[52] K. Holliger and J. A. Goff, "A generalised model for the 1/f-scaling nature of seismic velocity fluctuations," in *Heterogeneity in the Crust and Upper Mantle—Nature, Scaling, and Seismic Properties*, J. Goff and K. Holliger, Eds. Boston, MA, USA: Kluwer, 2003, pp. 131–154.
[53] A. W. Western and G. Blöschl, "On the spatial scaling of soil moisture," *J. Hydrol.*, vol. 217, no. 3/4, pp. 203–224, Apr. 1999.
[54] C. Schmelzbach, J. Tronicke, and P. Dietrich, "High-resolution water content estimation from surface-based ground-penetrating radar reflection data by impedance inversion," *Water Resourc. Res.*, vol. 48, no. 8, 2012, Art. ID. W08505.
[55] J. Irving and K. Holliger, "Geostatistical inversion of seismic and ground-penetrating radar reflection images: What can we actually resolve?" *Geophys. Res. Lett.*, vol. 37, no. 21, Nov. 2010, Art. ID. L21306.

Cedric Schmelzbach received the M.Sc. degree in geography with emphasis on applied geophysics from the University of Zurich, Zurich, Switzerland, and the Swiss Federal Institute of Technology (ETH), Zurich, in 2002 and the Ph.D. degree from Uppsala University, Uppsala, Sweden, and Rice University, Houston, TX, USA, in 2007, working on seismic reflection and seismic refraction investigations of the crystalline crust.

He was a Postdoctoral Researcher with the University of Potsdam, Potsdam, Germany, working on quantitative ground-penetrating radar imaging and signal processing for hydrogeophysical applications, before joining the PHASE consortium at Freie Universitaet Berlin, Berlin, Germany, to work on microseismic reflection imaging. He is currently a Senior Research Scientist with ETH Zurich, working in the framework of the industry-financed CARNEVAL consortium to work on geophysical multimethod investigations to study and remove the near-surface impact on seismic exploration data.

Dr. Schmelzbach is member of the Society of Exploration Geophysicists, the European Association of Geoscientists and Engineers, the German Geophysical Society (DGG), and the American Geophysical Union.

Emanuel Huber received the M.Sc. degree in environmental engineering from the Swiss Federal Institute of Technology (ETH) Zurich, Zurich, Switzerland, in 2009. He is currently working toward the Ph.D. degree in Earth sciences at the University of Basel, Basel, Switzerland.

His research focuses on the characterization and modeling of coarse braided river deposits, more particularly on the relationship between the surface morphology and the subsurface heterogeneity.